EXAFS analysis of Ru265 and Ru360 in human blood

Ani T. Baker,[a†] James H. Lovett,[a†] Haipei Zou,[b,c] Justin J. Wilson,[b,c] Hugh H. Harris[a*]

[a] Discipline of Chemistry, The University of Adelaide, North Terrace, Adelaide, SA 5005, Australia
E-mail: hugh.harris@adelaide.edu.au
[b] Department of Chemistry and Biochemistry, University of California Santa Barbara, Santa Barbara, CA, USA. (current affiliation)
[c] Department of Chemistry and Chemical Biology Cornell University, Ithaca, NY, USA
[†] These authors contributed equally.

Abstract

The dinuclear ruthenium (Ru) compounds, Ru265 and Ru360, are inhibitors of the mitochondrial calcium uniporter (MCU) and potential therapeutic agents for conditions associated with mitochondrial calcium (mt-Ca^{2+}) dysregulation. The nitrido-bridged Ru265 offers improved cell permeability and redox stability relative to the oxo-bridged analogue, Ru360, whilst maintaining high selectivity and potency. In this study, extended X-ray absorption fine structure (EXAFS) spectroscopy interrogated the stability of these compounds in buffer, saline solutions, and human blood, by probing the sensitive Ru—X—Ru scattering signal. Both dinuclear compounds remained intact in pH 7.4 buffered solution, even in the presence of glutathione. Following addition to whole blood, EXAFS showed the presence of diaqua-capped Ru265', indicating axial ligand substitution but stability of the Ru—N—Ru backbone during incubation (1 h, 37 °C). In contrast, Ru360 rapidly degraded in saline/DMSO at room temperature, as evidenced by the diminished intensity of the Ru···Ru peak in the EXAFS Fourier transform at ~3.65 Å. Subsequently, the mononuclear Ru360 degradation products displayed negligible uptake into red blood cells. These findings support previous studies which highlight the improved stability of Ru265 and provide validation of the structure and coordination environment of the complex in an *ex vivo* human blood sample.

Key words: ruthenium, mitochondrial calcium uniporter, human blood, stability, X-ray absorption spectroscopy

1 Introduction

Mitochondrial calcium (mt-Ca^{2+}) homeostasis is closely associated with the regulation of many critical biological processes, as intracellular Ca^{2+} flux modulates the production of adenosine triphosphate (ATP), impacting subsequent cellular metabolism, and can act to reinforce the initiation of cell death.[1-3] Transport of Ca^{2+} into the mitochondria in mammalian cells is mediated by the mitochondrial calcium uniporter (MCU) complex, which consists of multiple inner-membrane spanning subunits functioning together with mt-Ca^{2+} uptake proteins 1 and 2 (MICU1 and MICU2) in the intermembrane space.[4] Dysregulation of mt-Ca^{2+} and subsequent Ca^{2+} overload can stimulate overproduction of reactive oxygen species (ROS). Simultaneously, ROS can mediate sensitisation of the mitochondrial permeability transition pore (mPTP) to Ca^{2+}-mobilising agonists, further perturbing the flux of mt-Ca^{2+}.[5] Excess mt-Ca^{2+} has also been associated with overexpression of the Ca^{2+}-activated protease calpain.[6] Overabundance of these species can culminate in cell damage and death. As such, mt-Ca^{2+} dysregulation has been implicated in the progression of various neurodegenerative diseases,[7-9] ischemic stroke,[10] cardiovascular disease,[11,12] and cancer.[13-15]

Following recognition of the role of mt-Ca^{2+} uptake in these pathophysiological conditions, a growing body of research has emerged focusing on the development of MCU inhibitors as tools to investigate the mechanisms of Ca^{2+} dysregulation and as potential therapeutic agents.[16-18] In recent

years, combinatorial screening strategies have been utilised to identify organic small-molecules with MCU-inhibitory properties.[19,20] However, these compounds and other small-molecule MCU inhibitors designed in the last two decades generally exhibit alternative biological activities, creating undesirable off-target effects and secondary toxicity.[21-25]

The most commonly utilised MCU inhibitor is ruthenium 360 (Ru360, **Scheme 1**), a dinuclear oxo-bridged Ru compound and derivative of ruthenium red (RuRed), with strong UV-visible absorbance at 360 nm.[26-28] This compound exhibits selective MCU-inhibitory activity with nanomolar potency in digitonin-permeabilised rat cardiomyocytes.[27] However, the widespread application of Ru360 in intact biological systems is significantly impeded by its natively poor cell permeability,[27,29] and unfavourable redox stability.[22] In contrast to Ru360, the nitrido-bridged analogue, Ru265 (**Scheme 1**), has been shown to inhibit MCU-mediated mt-Ca^{2+} uptake in intact HEK293T and HeLa cells,[21,30] demonstrating substantially greater cell permeability while retaining high selectivity and nanomolar potency. In addition, Ru265 was found to provide protection against mt-Ca^{2+} overload in an *in vivo* model of ischemic stroke.[6]

Recent experiments have demonstrated striking differences in the redox activity of Ru265 and Ru360 complexes.[22] In an aqueous environment, the axial chloride and formate ligands of Ru265 and Ru360 are replaced by water and/or hydroxide ligands (depending on the pH environment). These aquated complexes are denoted as Ru265' and Ru360' (**Scheme 1**). Cyclic voltammetry studies revealed that Ru360' possesses redox potentials within the range of reduction potentials for common biological reducing agents (-0.744 to +0.556 V vs. SCE), with an irreversible reduction occurring at -0.740 mV vs. SCE, whereas Ru265' shows no redox activity between -1 and +1 V vs. SCE.[22] Furthermore, investigations of cellular uptake mechanisms revealed that Ru265 uptake is mediated by the organic cation transporter 3 (OCT3),[22] which is widely distributed throughout most mammalian tissues, particularly in the heart, skeletal muscles, placenta, and brain.[31-33] In contrast, increased uptake of Ru360' was not observed in cells overexpressing OCT3, indicating that the oxo-bridged analogue is not an effective substrate for the transporter.[22] These findings provide valuable insight into the enhanced bioactivity of Ru265 *in vitro* and *in vivo*.

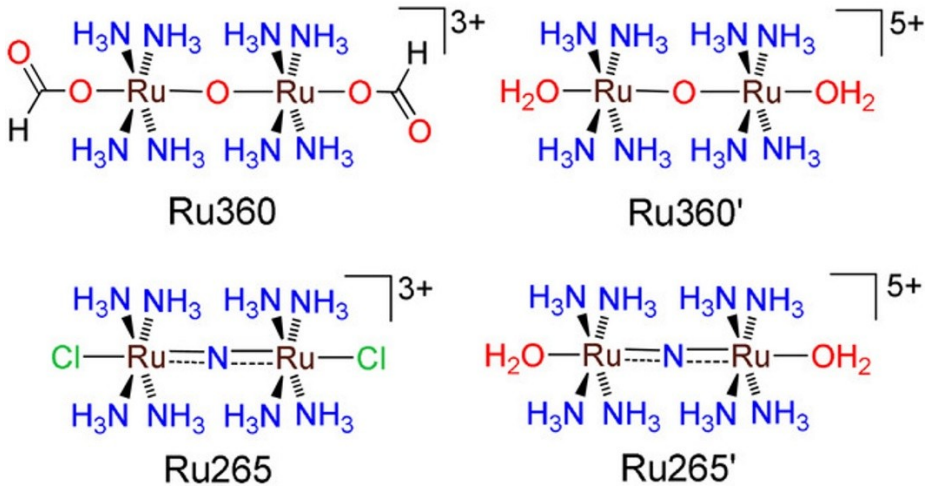

Scheme 1. Chemical structures of dinuclear Ru compounds discussed in this work. Note that the presence of axial water (H_2O) ligands for the aquated complexes, Ru265' and Ru360', is pH dependent. These ligands may be substituted for hydroxide (OH^-) ligands under physiological conditions.

Herein we describe further evaluation of the stability of Ru265 and Ru360 in biological buffers and in human whole blood using Ru K-edge extended X-ray absorption fine structure (EXAFS) spectroscopy. This synchrotron-based X-ray technique probes the characteristic absorption energies of core electrons. The unique oscillations arising from the interferences between the photoelectron

waves of the absorber and backscatterers provide structural information which can be used to characterise the coordination environment and bond distances between the absorber and neighbouring atoms. Unlike X-ray diffraction-based methods, EXAFS does not provide three-dimensional characterisation and interrogates only a limited radial field of view surrounding the central absorbing atom (up to ~5 Å), however, it offers high bond length accuracy, improved precision in atomic positions, and can be utilised to obtain structural information for metal complexes and metabolites in solution.[34,35] Thus, EXAFS analysis allows sensitive monitoring of the Ru—X—Ru backbone, a structural feature which is unique to these dinuclear Ru compounds, in aqueous environments. In addition, samples require minimal preparation and pre-treatment, preserving the native chemistry and translating to results which best represent the true Ru speciation directly following treatment.

In this work, Ru265 and Ru360 solutions were prepared in 3-(N-morpholino)propanesulfonic acid (MOPS) buffer at physiological pH (~7.4) in the presence and absence of *L*-glutathione (GSH, 5 molar equivalents) as a biological reducing agent. Whole blood was treated with 0.1 mM Ru265 or Ru360 from a 1 mM stock solution prepared in physiological saline (160 mM, pH ~7.4), containing 10% dimethyl sulfoxide (DMSO). Human whole blood serves as a valuable model system to evaluate biological stability, as drug compounds must first enter the bloodstream to be transported to other tissues to deliver therapeutic activity and undergo metabolic processing. Our EXAFS data demonstrates that Ru265 upholds appreciable stability in buffer and saline/DMSO solutions, and in human blood, whereas Ru360 undergoes rapid degradation in saline/DMSO at physiological pH and exhibits poor uptake into red blood cells (RBCs).

2 Materials and methods

2.1 Sample preparation

2.1.1 Synthesis of Ru265 and Ru360

The dinuclear Ru compounds Ru265 ($[Cl(NH_3)_4Ru(\mu\text{-}N)Ru(NH_3)_4Cl]Cl_3$ / $Cl_5H_{24}N_9Ru_2$) and Ru360 ($[(HCO_2)Ru(NH_3)_4(\mu\text{-}O)Ru(NH_3)_4(HCO_2)]Cl_3$ / $C_2H_{26}Cl_3N_8O_5Ru_2$) were synthesised and characterised according to previously described procedures.[21,36]

2.1.2 Standards in biological buffers

A stock solution of containing 50 mM 3-(N-morpholino)propanesulfonic acid (MOPS, M1254, Sigma-Aldrich) was prepared in ultrapure deionised water from a Milli-Q water purification system (Millipore-Waters, Australia). The pH of the solution was adjusted to ~7.4 with aqueous sodium hydroxide (NaOH, 1 M). Using this buffered solution, standards containing Ru265 (2 mM) and Ru360 (5 mM) were prepared with and without the addition of 5 molar equivalents of *L*-glutathione (GSH, G4251, Sigma-Aldrich) incubated with the compounds at room temperature for 2.5 h. Aliquots (~100 µL) of each solution were injected into plastic sample holders covered with Kapton tape and immediately flash-frozen in liquid nitrogen (LN2) prior to placing the sample in the beamline for measurement.

2.1.3 Standards in saline/DMSO

Physiological saline solution containing 160 mM sodium chloride (NaCl) was prepared in ultrapure deionised (Milli-Q). The pH of the solution was adjusted to ~7.4 with aqueous sodium hydroxide (NaOH, 1 M). Ru265 and Ru360 were dissolved in dimethyl sulfoxide (DMSO, DA013, Chem-Supply) to prepare a 10 mM stock solution, which was then diluted by a factor of ten with physiological saline, for a final concentration of 1 mM (containing 10% DMSO). Aliquots (~100 µL) of each saline/DMSO

solution prepared as described above and stored at -80 °C until analysis. To complement EXAFS data, ^{1}H NMR and UV-Vis spectra were collected for a solution of Ru265 in saline/DMSO (10% DMSO-d6 or DMSO, 80 mM or 160 mM NaCl, pH 7.4), immediately after dissolution and following incubation at 37 °C for 4 h (characterisation summarised in SI, pages 1-2, **Figures S1** and **S2**).

2.1.4 Human blood samples

Blood was collected with informed consent from a volunteer participant (22 years old, biological male). Experiments were conducted with protocols and conditions approved by The University of Adelaide Human Research Ethics Committee (Approval Number: H-2024-155). Human whole blood was collected in 9 mL lithium heparin-coated vacutainers (Vacuette, Greiner Bio-One) and stored on ice before use (~1 h). Whole blood (900 µL) and Ru265 and Ru360 treatment solutions in saline/DMSO were preheated to 37 °C for ~15 min. The treatment solutions (100 µL) were then added to the whole blood and incubated at 37 °C for 1 h, to give a final concentration of 100 µM and 1% DMSO in the blood sample.

Following incubation, treated whole blood (700 µL) was separated into plasma and red blood cell fractions via centrifugation (10,000 rpm, 10 min, 20 °C). The plasma supernatant was isolated, and the RBC pellets were lyophilised under vacuum pressure at -55 °C. Plasma and whole blood samples (~100 µL) were injected into plastic sample holders covered with Kapton tape, immediately flash-frozen in LN2, and stored at -80 °C until analysis. The RBCs were packed into sample holders as dry powders and stored under the same conditions.

2.2 X-ray absorption spectroscopy

2.2.1 EXAFS data collection

Ru K-edge X-ray absorption spectra were recorded on the X-ray absorption spectroscopy (XAS) beamline at the Australian Synchrotron (Clayton, Victoria, Australia) with a storage ring containing ~200 mA at 3.0 GeV. The incident X-ray beam was sourced from a 1.9 T wiggler insertion device and selected using a Si(111) double crystal monochromator with an energy resolution ($\Delta E/E$) of ~1.5×10^{-4}. Rhodium-coated Kirkpatrick–Baez mirrors upstream of the sample were used to achieve rejection of higher order harmonics and to deliver a focused beam of ~250 µm^2. All standards and samples were measured in fluorescence mode using a detector oriented at 90° to the incident beam to minimise background noise from scattered photons. The standards prepared in MOPS buffer were analysed using a 100-element Ge detector (UniSys, Canberra, Australia), and measurements for the standards in saline/DMSO and blood samples were obtained using an 18-element Ge detector (Mirion, France). To minimise radiation damage and thermal fluctuations contributing to the Debye-Waller factor for EXAFS analysis, the samples were maintained at ~10 K using a helium pulsed expansion cooled cryostat (Oxford Instruments, Abingdon, UK). The Ru K-edge was monitored in between scans interrogating a single spot to assess radiation damage. No evidence of photodamage was observed between the first and last scans for each sample. The spectrum of a Ru foil, recorded in transmission downstream from the sample, was used as an internal standard to calibrate the energy for the first peak of the first derivative of the elemental Ru K-edge (22,118 eV).

2.2.2 EXAFS data analysis

The EXAFS oscillations $\chi(k)$ were quantitatively analysed by curve-fitting using the EXAFSPAK suite of computer programs (G. N. George, SSRL, http://ssrl.slac.stanford.edu/exafspak.html).[37] Fourier transforms were phase-corrected for a Ru absorber (Z_{abs} = 44) and N backscatterer (Z_{bsc} = 7). The threshold energy E_0 was assumed to be 22,135 eV, and *ab initio* theoretical phase and amplitude

functions were calculated using the program FEFF version 8.5L.[38] FEFF multiple scattering calculations from the heavy atom framework were computed using the optimised geometries from previously published crystallographic data.[21,22,36] Prior to pre-edge subtraction, spline fitting, and extraction of EXAFS oscillations, the *k*-range for spectra from each sample was trimmed to 12.5 $Å^{-1}$ or 15.0 $Å^{-1}$, as necessary according to the data quality and original range. Generally, k_{max} = 12.5 $Å^{-1}$ was chosen due to increasingly poor signal-to-noise in spectra collected from biological samples above *k* = 13.0 $Å^{-1}$. Calculated scattering paths included a maximum N_{leg} path = 6 and R_{max} = 6.0 Å.

During EXAFS fitting, the Ru—N/O(bridging atom) single scattering path was linked to the single scattering and multiple scattering paths for the Ru···Ru interaction, hence the bond lengths (R) and/or Debye-Waller (σ^2) parameters were floated simultaneously for these components. In these cases, the Debye-Waller factors for the Ru—N/O(bridging atom) and the Ru···Ru scattering interaction were maintained in an approximately 1:2 ratio. Note that the coordination number (N) for Ru···Ru scattering is given as '1,2,1', referring to (i) the single scattering (two-legged) path '020', (ii) the doubly degenerate three-legged multiple scattering paths '0210' and '0120' (asymmetric equivalents), and (iii) the four-legged multiple scattering path '01210', respectively, where 0 = Ru (origin), 1 = bridging N or O atom, and 2 = neighbouring Ru atom. These three components remained linked in all fits, with equivalent R and σ^2 parameters. Debye-Waller factors below the typical chemically reasonable lower limit of 0.0015 $Å^2$ were accepted for the Ru—N/O(bridging atom) components given the rigidity of the Ru—X—Ru backbone. In samples where degradation of this backbone was evident, the Ru—N/O(bridging atom) '010' single scattering path was unlinked from the Ru···Ru single and multiple scattering paths (020, 0210, and 01210) , hence these components were optimised independently. Degenerate paths for the Ru—N (NH_3) single scattering interactions were combined as one component with N = 4. During EXAFS fit refinement, components contributing less than 0.75% towards the overall fit were excluded.

3 Results and discussion

3.1 EXAFS curve-fitting of Ru compounds in biological buffers

The phase-corrected Fourier transforms of these dinuclear Ru compounds are dominated by a single scattering peak at ~2.11 Å derived from the degenerate Ru—N paths representing the four ammine (NH_3) ligands coordinated to the absorber Ru atom (**Figure 1**). Major features also arise from the single scattering interactions between the absorber and the bridging N or O atom and the multiple scattering paths across to the neighbouring Ru atom in the backbone. In Ru265, the Ru—N bridge distance is ~1.74 Å. This distance is longer for the Ru—O bridge in Ru360, at ~1.82 Å. Importantly, the Ru···Ru scattering interactions give rise to distinctive structure in the EXAFS oscillations, beginning at around *k* = 7 $Å^{-1}$, producing peaks in the Fourier transform at ~3.48 Å and ~3.65 Å for Ru265 and Ru360, respectively. This distinguishable feature affords valuable sensitivity in the determination of the stability of these dinuclear compounds in biological mixtures, as the presence or absence of the Ru—X—Ru backbone can be readily identified in the EXAFS oscillations. Individual EXAFS plots and deconvolutions (indicating the contributions from the main scattering components) for Ru265 and Ru360 standards are provided in the Supplementary Information (SI **Figures S3-S6**).

3.1.1 Ru265

Ab initio multiple scattering calculations were carried out in FEFF for Ru265 using structural information from existing crystallographic models for Ru265 (dichlorido-capped) and Ru265' (diaqua-capped).[21,22] However, we note that at physiological pH (above pK_{a2} = 7.00), Ru265' exists as a combination of the aqua/hydroxido-capped and dihydroxido-capped species.[22]

The best fit to the EXAFS data for Ru265 in MOPS was obtained using the Ru265 model with axial Cl ligands (**Table 1**, **Figure 1A**, and **Figure S3**). In the buffered solution, the Ru—Cl bond distance was optimised at ~2.44 Å. This is relatively longer than the interatomic distance of ~2.38 Å given in the crystallographic model,[21] however, it is not unreasonable and lies within the range of Ru—Cl bond distances (2.30 – 2.48 Å) calculated by computational methods in other literature.[39] The presence of axial Cl ligands was anticipated given the short preparation time for the sample and the ~45 min aquation half-life of the Ru265 at room temperature.[22] Other interatomic distances, including the Ru—N_{br} (bridging μ–N^{3-}, 1.74 Å), Ru···Ru (3.48 Å), and Ru—N (NH_3, 2.11 Å) (**Table 1**), show good agreement with the existing model (R ± 0.006 Å or better), confirming the stability of the compound in this medium. Floating the Debye-Waller factor for Ru—N (NH_3) resulted in a value converging around 0.0013 $Å^2$. The rigidity of the Ru—X—Ru backbone provides some exception to the typical lower limits for the Debye-Waller factor (0.0015 $Å^2$), however, this low value does not provide a realistic representation of the thermal disorder corresponding to the NH_3 ligands. These ligands are substantially more labile; hence, the Debye-Waller value was constrained to a chemically reasonable limit. The greater intensity of the ~2.11 Å peak may be attributed to some contributions from Ru—O interactions (as H_2O/OH^- ligands, at ~2.14 Å) derived from a small proportion of aquated Ru265'. Fitting to a mixture of both dichlorido- and diaqua-capped models (80:20 ratio) was attempted, however, the statistical goodness-of-fit for this mixed model was equivalent to that obtained from fitting with the dichlorido-capped model alone. This was consistent at varying *k*-ranges (k_{max} = 12.5, 14, and 15.5 $Å^{-1}$) and when fitting in either *k*-space or *R*-space. Additionally, the bond resolution ($\Delta R = \pi/2\Delta k$) at k = 12.5 $Å^{-1}$ is ~0.14 Å and improves only marginally to ~0.11 Å at k = 15.0 $Å^{-1}$, thus, an axial $H_2O/^-OH$ ligand cannot be resolved from the equatorial NH_3 ligands, and the presence and intensity of the 2.44 Å peak indicates that dichlorido-capped species is the dominant form.

In the Ru265 MOPS standard incubated with GSH for 2.5 h, EXAFS data suggests that the dinuclear complex remains intact, however, in this time frame, the Cl ligands were replaced by O-containing ligands (H_2O and/or OH^- ligands). This is evidenced by the absence of the ~2.44 Å peak in the Fourier transform for this sample in **Figure 1A** (and **Figure S4**) and aligns with expectations based on the aquation half-life. The axial Ru—O component was optimised at a bond length of ~2.15 Å, which aligns well with the crystallographic model.[22] Excluding this distinction derived from axial ligand substitution, the interatomic distances of Ru—N_{br} (bridging μ–N^{3-}, 1.74 Å), Ru···Ru (3.48 Å), and Ru—N (NH_3, 2.10 Å) remain consistent with the EXAFS data from Ru265 in MOPs without GSH (**Table 1**), hence, the presence of this biological reducing agent does not influence the stability of the complex under these conditions (5 molar equivalents, 2.5 h, pH ~7.4).

3.1.2 Ru360

For Ru360 samples in MOPS buffer, *ab initio* multiple scattering calculations in FEFF were performed using the crystallographic model for the aquated Ru360 complex (Ru360') where the axial formate ligands are substituted by OH^- groups.[36] These formate ligands undergo rapid aquation, at a rate faster than that observed for the dichlorido-capped Ru360 analogue.[26,36] Previous studies have demonstrated that this substitution does not impede MCU-inhibitory activity.[15,22] Furthermore, Ru360' exists almost exclusively as the dihydroxido-capped species at physiological pH, given the low pK_a values for the complex (pK_{a1} = 2.98 and pK_{a2} = 4.75).[22]

Using the Ru360' model, similar fit-errors were obtained for Ru360 in MOPS with and without GSH (~34% and ~36%, respectively). For both samples, the interatomic distances determined by EXAFS curve-fitting were relatively consistent with the expected bond lengths based on the crystallographic data; Ru—O_{br} (bridging μ–O^{2-}, 1.82–1.84 Å), Ru···Ru (3.64–3.67 Å), Ru—N (NH_3, 2.10–

2.13 Å), and Ru—O (OH^-, 2.03–2.06 Å) (**Table 1**, **Figure 1B**, and **Figures S5-S6**). Whilst these values show comparatively poorer precision relative to the Ru265 samples, and greater deviation from each other and the Ru360' model (± 0.03 Å), the EXAFS data substantiates the presence of the Ru—O—Ru backbone in both samples. In addition, the ~1:2 proportionality between the Debye-Waller factors for Ru—O_{br} and Ru···Ru scattering interactions were maintained for both samples. Thus, like the N-bridged analogue Ru265, this data demonstrates that Ru360' is stable in 50 mM MOPS with and without the addition of GSH as a reducing agent under the present conditions (5 molar equivalents, 2.5 h, pH ~7.4). However, this treatment was a relatively short and conducted at room temperature. Previous data indicates a time-dependent loss in MCU-inhibitory activity in permeabilised HeLa cells for Ru360' when prepared under similar conditions (10 μM Ru360' in 50 mM MOPS at pH 7.4 with 2 mM GSH) but incubated at physiological temperature (37 °C).[22] Similar loss of activity was also observed upon incubation of Ru360' with 250 μM sodium ascorbate, with total loss of inhibitory activity observed after 24 h of incubation with either GSH or ascorbate. Additionally, incubation with stronger reducing agents (sodium sulfite and sodium dithionite) resulted in complete loss of MCU-inhibitory function after 2 h.[22] The structures of these reduced metabolites in biological media have not yet been characterised.

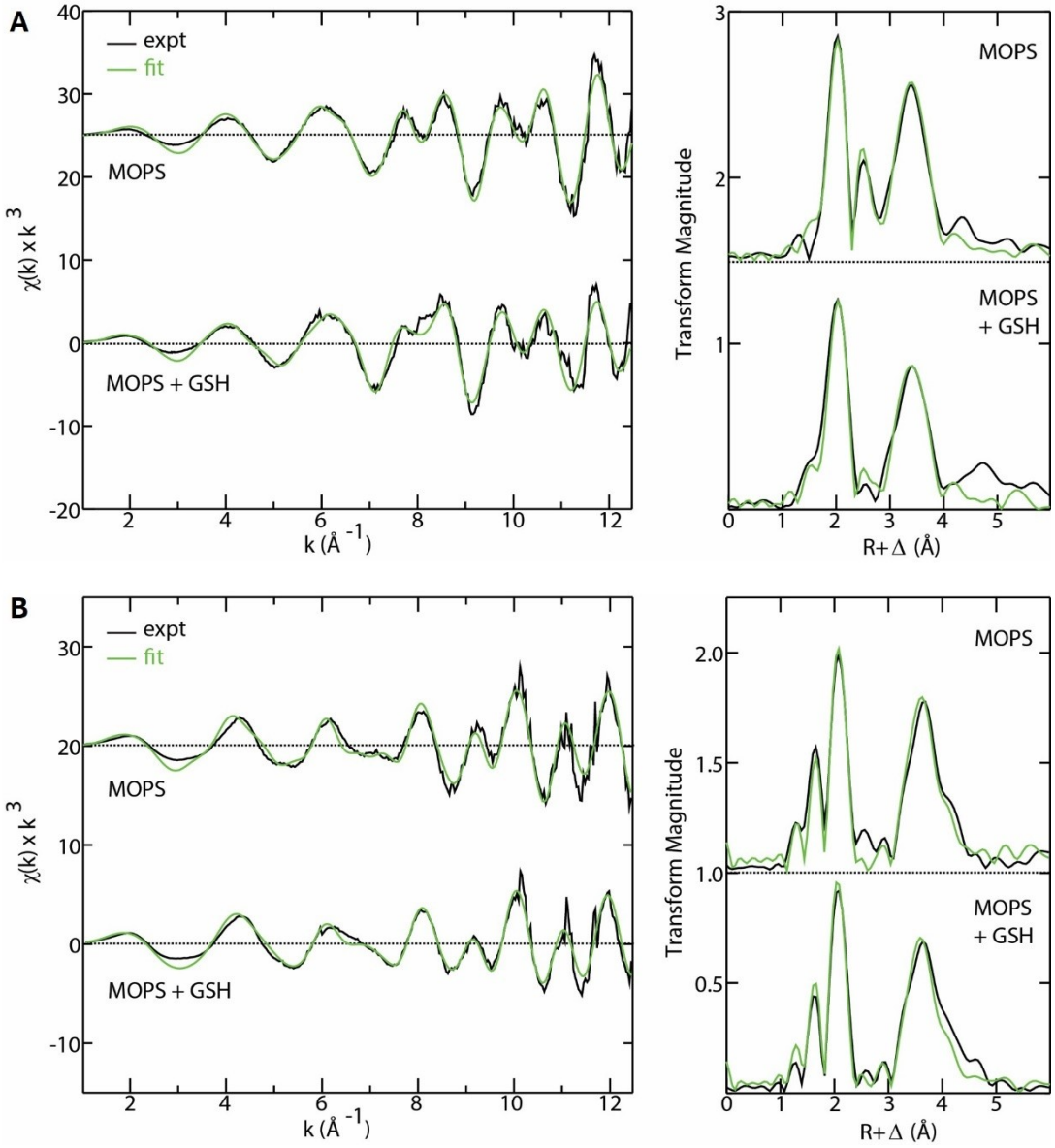

Figure 1. Results of EXAFS curve fitting for (**A**) Ru265 and (**B**) Ru360 standards in biological buffers, showing the EXAFS oscillations to k_{max} = 12.5 $Å^{-1}$ (left panel) and the corresponding Fourier transform phase corrected for Ru—N backscattering (right panel). The experimental data (solid black line) and best fit (solid green line) are

overlayed for each spectrum. Data for standards prepared in 50 mM MOPS buffer (pH ~7.4) with and without 5 molar equivalents of GSH are plotted offset from one another (origin indicated by dashed black lines). Corresponding curve fitting parameters are provided in **Table 1**.

Table 1. EXAFS curve-fitting parameters for Ru265 and Ru360 standards in biological buffers;[a] 2 mM Ru265 and 5 mM Ru360 in 50 mM MOPS with/without 5 molar equivalents of GSH. All standards were prepared at pH ~7.4.

Standard	Path[b]	N	R (Å)	σ^2 (Å^2)	ΔE_0 (eV)	F[c]
Ru265 in MOPS	Ru—N_{br}	1	1.740(1)	0.00113(9)[d]	-4.9(2)	0.2793
	Ru···Ru	1,2,1	3.480(1)	0.00208(9)		
	Ru—N	4	2.106(1)	0.0015[e]		
	Ru—Cl	1	2.436(4)	0.0034(4)		
	+9 additional unlisted single and multiple scattering shells[f]					
Ru265 in MOPS + GSH	Ru—N_{br}	1	1.739(1)	0.0015(2)	-4.9(3)	0.3930
	Ru···Ru	1,2,1	3.477(1)	0.0030(2)		
	Ru—N	4	2.091(2)	0.0031(2)		
	Ru—O	1	2.15(1)	0.004(1)		
	+7 additional unlisted single and multiple scattering shells[f]					
Ru360 in MOPS	Ru—O_{br}	1	1.828(1)	0.0013(1)[d]	-5.4(3)	0.3646
	Ru···Ru	1,2,1	3.666(1)	0.0027(1)		
	Ru—N	4	2.128(4)	0.0058(4)		
	Ru—O	1	2.059(8)	0.0023(6)		
	+7 additional unlisted single and multiple scattering shells[f]					
Ru360 in MOPS + GSH	Ru—O_{br}	1	1.817(1)	0.0017(1)	-6.6(3)	0.3446
	Ru···Ru	1,2,1	3.640(1)	0.0034(1)		
	Ru—N	4	2.100(3)	0.0057(3)		
	Ru—O	1	2.031(7)	0.0044(8)		
	+8 additional unlisted single and multiple scattering shells[f]					

[a] Coordination numbers (N), interatomic distances (R), Debye-Waller factors (σ^2, mean-square deviations in interatomic distance), and threshold energy shifts (ΔE_0). The values in parentheses are the estimated standard deviations in the last digit obtained from the diagonal elements of the covariance matrix. Note that the accuracies are somewhat larger than the precisions, typically ± 0.02 Å for R and ± 20% for N and σ^2.

[b] All paths terminate at the originating Ru atom (not indicated). Note that EXAFS cannot readily distinguish between scatterers of similar atomic number (e.g. S/Cl or N/O). Assignments of Ru—N (from NH_3) ligands and Ru—O (from H_2O or OH^- axial ligands) are based on the consistency of N and R with the crystallographic models.

[c] The fit-error function (F) is defined by $F = \left(\sum k^6 \left(\chi(k)_{cald} - \chi(k)_{expt}\right)^2 / \sum \chi(k)^2_{expt}\right)^{1/2}$, where $\chi(k)$ are the EXAFS oscillations and k is the photoelectron wavenumber given by $k = \left(\left(2 m_e/\hbar^2\right)\left(E - E_0\right)\right)^{1/2}$.

[d] Debye-Waller factor below the typical chemically reasonable lower limit of 0.0015 Å^2 is accepted for these features given the rigidity of the Ru—N—Ru and Ru—O—Ru backbones.

[e] For Ru—N (NH_3), the Debye-Waller factor was constrained to the chemically reasonable lower limit (0.0015 Å^2). Unconstrained the value converged at 0.0013 Å^2.

[f] Paths include the single scattering path Ru···N (NH_3 ligands on adjacent Ru atom) and multiple scattering paths to the distant axial ligand across the Ru—N—Ru and Ru—O—Ru backbones.

3.2 Stability of Ru compounds in saline/DMSO and human blood

Prior to incubation in human blood, 1 mM solutions of Ru265 and Ru360 were prepared in physiological saline (160 mM, pH ~7.4) containing 10% DMSO. Although potentially unnecessary given the low treatment concentrations and solubilities of these Ru compounds, DMSO is a widely

used polar aprotic solvent in biomedical applications due to its ability to alter biological lipid membranes,[40] acting to enhance the membrane penetration of various compounds and drugs.[41,42] Whilst the influence of DMSO on the cellular uptake of Ru265 and Ru360 was not directly evaluated in this work, the EXAFS data reveals some interesting structural changes to the complexes under these solvent conditions prior to and following incubation in blood.

3.2.1 Ru265 in saline/DMSO

The best fit for Ru265 in saline/DMSO was obtained using the dichlorido-capped model (**Table 2**, **Figure 2A**, and **Figure S7**). Consistent with the EXAFS data for Ru265 in MOPS, the Ru—Cl bond distance was optimised at ~2.42 Å. In EXAFS analysis, backscatterers with similar atomic numbers such as S and Cl cannot be readily distinguished, hence, it is also possible that the axial Cl ligands may be replaced by S-coordinated DMSO (κ*S*-DMSO). However, existing literature reports shorter bond distances for Ru—κ*S*-DMSO, between ~2.24 Å and ~2.30 Å.[43-45] Notably, these interatomic distances were determined for a variety of mononuclear Ru complexes coordinated with sulfoxides and other ligands including NH_3, Cl, and bipyridine, hence, the electron density and unique geometry of the dinuclear Ru265 complex may permit coordination of DMSO (via the S atom) at a longer bond distance. Notwithstanding this uncertainty, the interatomic distance determined by EXAFS analysis more closely aligns with the bond length determined for Ru265 by X-ray crystallography,[21] and with other reported Ru—Cl bond distances in various mononuclear Ru complexes (between ~2.37 Å and ~2.44 Å).[43,44] Moreover, the bond lengths for Ru—N_{br} (bridging μ–N^{3-}, 1.74 Å), Ru···Ru (3.48 Å), and Ru—N (NH_3, 2.11 Å) (**Table 2**) are consistent with the existing Ru265 model, indicating that the complex is stable in physiological saline and 10% DMSO.

Furthermore, ^{1}H NMR spectra of Ru265 in saline/DMSO (**Figure S1**) show that the NH_3 peak splits after 4 h incubation in 10% DMSO-d_6 and 80 mM saline (pH 7.4) at 37°C, corresponding to solvation/aquation and exchange of the axial ligands. In addition, proton NMR data provides no evidence of decomposition of Ru265 into mononuclear species (see SI pages 1-2 for further details). This is also supported by UV-Vis data (**Figure S2**) which indicates that the 265 nm absorbance band is retained following incubation in 10% DMSO and 160 mM saline (pH 7.4, 37°C, 4 h). The slight blue shift and decreased intensity is consistent with previous reports of axial ligand exchange in aqueous solution.[22] Thus, the additional proton NMR and UV-Vis spectroscopy data corroborate our interpretations from Ru K-edge EXAFS analysis.

3.2.1 Ru360 in saline/DMSO

In contrast, EXAFS data demonstrates that Ru360 undergoes rapid decomposition (within ~1 h during sample preparation) at room temperature in 160 mM saline in the presence of 10% DMSO, as evidenced by the greatly diminished intensity of the Ru···Ru peak at ~3.65 Å (**Table 2**, **Figure 2B** and **Figure S8**). Subsequently, the Ru—O(bridging μ–O^{2-}, 1.81 Å) and Ru···Ru paths were unlinked and floated independently. The Debye-Waller factors for these paths converged at 0.0055 Å^2 and 0.0076 Å^2 (**Table 2**), respectively, emphasising the weakened contributions and greater disorder associated with these scattering interactions. For this sample, *ab initio* calculations in FEFF were performed using a modified Ru360' model where the axial OH^- ligands were replaced by S/Cl atoms. The bond distance for this Ru—S/Cl interaction was optimised as ~2.37 Å. This interatomic distance is longer than previously reported values for Ru—κ*S*-DMSO,[43-45] and aligns better with a typical Ru—Cl bond length, albeit towards the minimum length for this interaction as reported in the literature.[43,44] However, this distance is notably shorter than the Ru—Cl distances determined for Ru265 in MOPS and saline/DMSO. Following degradation of the Ru—O—Ru backbone, there are many possible

coordination environments for mononuclear Ru species, therefore, the sample likely contains a complex mixture of mononuclear Ru species with different combinations of ligands (N/O and S/Cl).

Due to the paramagnetic behaviour of Ru360, ^{1}H NMR spectra of this complex incubated in saline/DMSO were not obtained. Ru K-edge EXAFS data provides clear evidence of decomposition into mononuclear Ru species. Although this work does not focus on characterisation of these degradation products, an initial attempt to decipher the mixture of coordination environments is explored further in the EXAFS analysis of Ru360 in whole blood, described below.

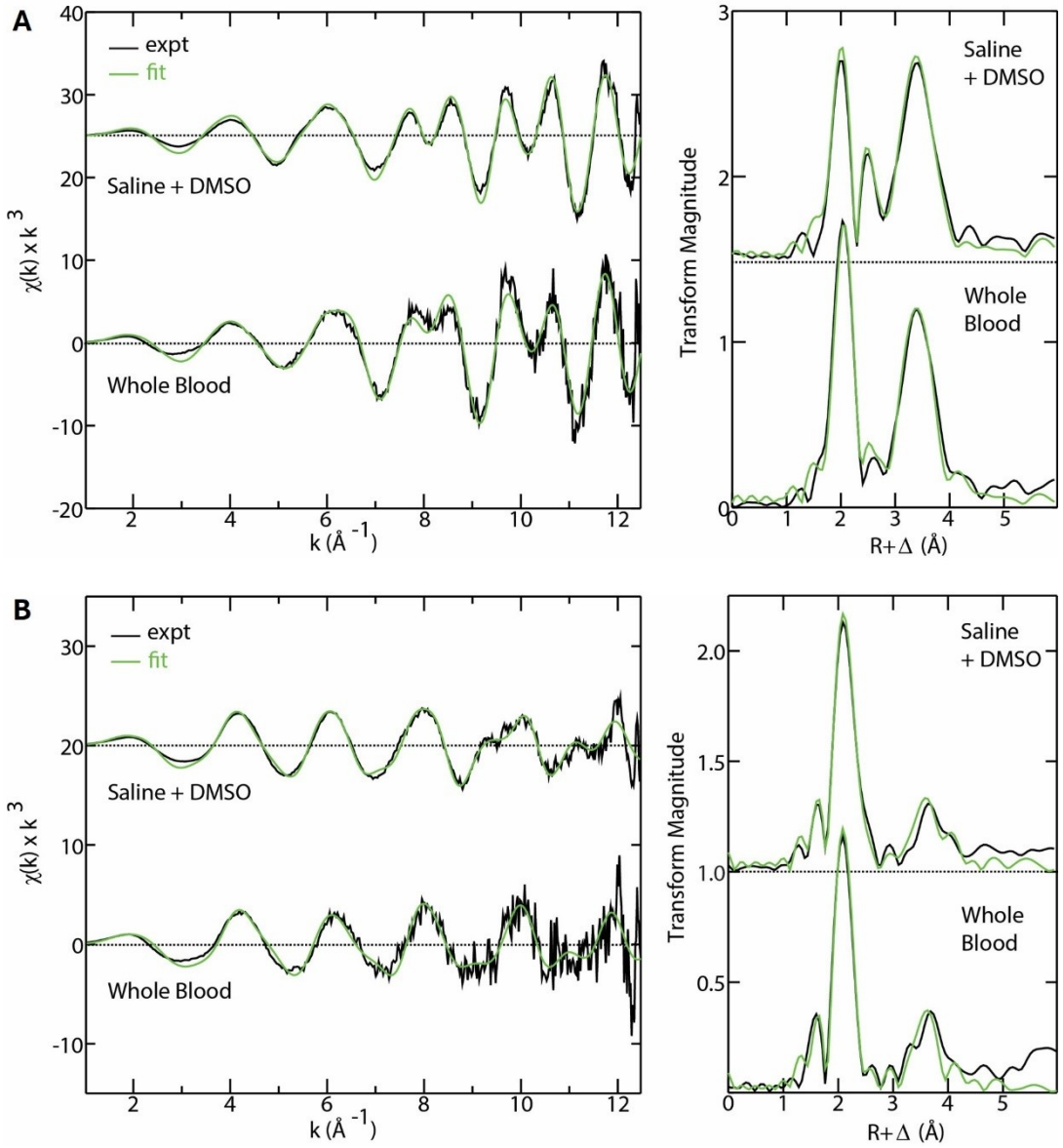

Figure 2. Results of EXAFS curve fitting for (**A**) Ru265 and (**B**) Ru360 standards in saline/DMSO and whole blood, showing the EXAFS oscillations to k_{max} = 12.5 Å^{-1} (left panel) and the corresponding Fourier transform phase corrected for Ru—N backscattering (right panel). The experimental data (solid black line) and best fit (solid green line) are overlayed for each spectrum. Data for standards prepared in 160 mM saline and 10% DMSO (pH ~7.4) and the 10X dilution in whole blood are plotted offset from one another (origin indicated by dashed black lines). Corresponding curve fitting parameters are provided in **Table 2** and **Table 3** (data shown for Ru360 in whole blood represents Fit B).

Table 2. EXAFS curve-fitting parameters for Ru265 and Ru360 standards in saline/DMSO;[a] 1 mM Ru265 or Ru360 in 160 mM saline with 10% DMSO. All standards were prepared at pH ~7.4.

Standard	Path[b]	N	R (Å)	σ^2 (Å^2)	ΔE_0 (eV)	F[c]
Ru265 in saline + 10%	Ru—N_{br}	1	1.740(1)	0.00069(7)[d]	-6.5(2)	0.2700

DMSO	Ru···Ru	1,2,1	3.478(1)	0.00139(7)[d]		
	Ru—N	4	2.106(2)	0.0016(2)		
	Ru—S/Cl	1	2.418(3)	0.0023(3)		
	+8 additional unlisted single and multiple scattering shells[e]					
Ru360 in saline + 10% DMSO	Ru—O_{br}	1	1.814(5)	0.0055(7)	-6.1(3)	0.3816
	Ru···Ru	1,2,1	3.651(4)[f]	0.0076(3)[f]		
	Ru—N	4	2.115(1)	0.0022(1)		
	Ru—S/Cl	1	2.369(3)	0.0029(2)		
	+13 additional unlisted single and multiple scattering shells[e]					

[a] Coordination numbers (N), interatomic distances (R), Debye-Waller factors (σ^2, mean-square deviations in interatomic distance), and threshold energy shifts (ΔE_0). The values in parentheses are the estimated standard deviations in the last digit obtained from the diagonal elements of the covariance matrix. Note that the accuracies are somewhat larger than the precisions, typically ± 0.02 Å for R and ± 20% for N and σ^2.

[b] All paths terminate at the originating Ru atom (not indicated). Note that EXAFS cannot readily distinguish between scatterers of similar atomic number (e.g. S/Cl or N/O). Assignments of Ru—N (from NH_3) ligands and Ru—O (from H_2O or OH^- axial ligands) are based on the consistency of N and R with the crystallographic models.

[c] The fit-error function (F) is defined by $F = \left(\sum k^6 \left(\chi(k)_{cald} - \chi(k)_{expt}\right)^2 / \sum \chi(k)^2_{expt}\right)^{1/2}$, where $\chi(k)$ are the EXAFS oscillations and *k* is the photoelectron wavenumber given by $k = \left(2m_e/\hbar^2\right)\left(E - E_0\right)\right)^{1/2}$.

[d] Debye-Waller factor below the typical chemically reasonable lower limit of 0.0015 $Å^2$ is accepted for these features given the rigidity of the Ru—O—Ru backbone.

[e] Paths include the single scattering path Ru···N (NH_3 ligands on adjacent Ru atom) and multiple scattering paths to the distant axial ligand across the Ru—O—Ru backbone.

[f] In this sample where the dinuclear Ru360 complex showed degradation, Ru—O_{br} was unlinked from Ru···Ru paths (1:2 proportionality in the Debye-Waller factor no longer maintained).

3.2.3 Ru265 in human blood

EXAFS data collected for Ru265 incubated in human whole blood indicates that the dinuclear complex remains intact under these treatment conditions with a short incubation period at physiological temperature and pH (0.1 mM, 1 h, 37 °C, pH ~7.4). EXAFS oscillations were best fit using the Ru265' (diaqua-capped) model,[22] indicating substitution of the axial Cl ligands during treatment as evidenced by the absence of the ~2.42 Å peak in the Fourier transform (**Figure 2A, Figure S9**). This was anticipated given the rapid aquation kinetics of Ru265 under these conditions ($t_{1/2}$ ≈ 2.3 min).[22] In this fit, the bond lengths for Ru—N_{br} (bridging *μ*–N^{3-}, 1.74 Å), Ru···Ru (3.48 Å), and Ru—N (NH_3, 2.11 Å) (**Table 3**) align well with the existing Ru265' model, however, Ru—O (from the axial H_2O/OH^- ligands) was fit at ~2.09 Å, shorter than the anticipated interatomic distance of ~2.14 Å.

An alternative fit (data not shown), replacing the axial O atom for S/Cl was attempted, however, when fixing the other bond distances to their expected values and floating the bond length for Ru—S/Cl, this value consistently converged at R ≈ 2.26 Å with a Debye-Waller factor above 0.008 $Å^2$, exceeding the typical chemically reasonable limit for thermal and vibrational disorder. According to existing literature, coordination between Ru and DMSO via S is unlikely to occur at interatomic distances less than 2.23 Å.[43-45] DMSO is an ambidentate ligand capable of coordinating to Ru via the O atom (Ru—κ*O*-DMSO) through σ- and π-donor interactions, however, literature reports Ru—κ*O*-DMSO distances between 1.80 Å and 2.10 Å.[45,46] Unsurprisingly, this range approaches the anticipated bond lengths for Ru—N (NH_3) and Ru—O (H_2O/OH^-) in Ru265. In this fit for Ru265 in whole blood, the Debye-Waller factor for Ru—N (NH_3) was constrained to 0.0015 $Å^2$ but converged at a lower value

(0.0012 $Å^2$), potentially indicating further contributions from another N/O species coordinated to the complex. Thus, whilst the Ru265' model provides a reasonable fit to the EXAFS data, the inability to distinguish between N and O backscatterers and the similar bond distances of NH_3, H_2O, and κ*O*-DMSO ligands creates ambiguity regarding the exact coordination environment of Ru265 in whole blood.

EXAFS curve-fitting of plasma and red blood cells (RBCs) from the Ru265 treatment, indicates consistent Ru speciation in both fractions, best fit using the Ru265' model (**Table S1**, **Figures S10-S11**). Moreover, the signal intensity for both blood fractions suggests appreciable uptake of Ru265' into RBCs. However, we note that the plasma fractions were likely contaminated with material from the erythrocytes, as treatment resulted in partial RBC haemolysis. This may be attributed to the presence of 1% DMSO, which is known to exhibit haemolytic effects (even at low concentrations),[47,48] and/or the toxicity of Ru265 at the provided dose (100 μM), which is above the concentrations utilised in previous cell-based experiments.[6,21,22,49]

3.2.4 Ru360 in human blood

As established above, the dinuclear Ru360 complex was degraded in the saline/DMSO solution prior to treatment. Hence, EXAFS data for the whole blood shows a similarly diminished Ru···Ru peak (**Figure 2A**, **Table 3**). To further interrogate the possible coordination environments of the mononuclear/dinuclear Ru species, three EXAFS fits with different combinations of ligands were attempted; (A) Ru360' model (4 × NH_3 ligands, 1 × OH^- ligand, and bridging μ–O^{2-}), (B) modified Ru360' model replacing the axial OH^- group with a S/Cl ligand, and (C) an alternative modified Ru360' model (3 × NH_3, 1 × OH^- or κ*O*-DMSO, 1 × S/Cl ligand, and bridging μ–O^{2-}) (**Table 3**, **Figures S12-S14**). Given the poor signal-to-noise and the degradation of the Ru—O—Ru backbone, the fit errors obtained for Ru360 in whole blood (~62%) were considerably larger than previous samples (≤ 38%). In each fit, the Ru—O(bridging μ–O^{2-}) and Ru···Ru paths converged at ~1.8 Å and ~3.7 Å, respectively. This lengthening of the Ru···Ru interatomic distance and the large Debye-Waller factors (≥ 0.007 $Å^2$) associated with this path support the presence of minimal dinuclear Ru360 remaining in the sample. Across the three fits, the Ru—N (NH_3) bond length was consistent with the Ru360' model at ~2.10–2.12 Å. In contrast, the interatomic distance calculated for Ru—S/Cl varies substantially between Fit B (~2.32 Å) and Fit C (~2.28 Å). These values are approaching the upper limit for reported Ru—κ*S*-DMSO interactions,[43-45] and are accompanied by large Debye-Waller factors (≥ 0.006 $Å^2$), providing unconvincing evidence for coordination to DMSO via S. Alternatively, potential DMSO coordination via O cannot be ruled out, as this interaction occurs between 1.80 Å and 2.10 Å,[45,46] overlapping with Ru—N/O distances for NH_3, OH^- and the bridging μ–O^{2-} in the dinuclear complex.

Alternatively, following addition to whole blood, mononuclear Ru species may undergo further reduction and/or ligand exchange, substituting labile DMSO, H_2O/OH^-, or Cl ligands for multidentate biological ligands such as *L*-methionine and *L*-cysteine groups derived from peptides and proteins. The binding affinities and coordination of these amino acids to Ru(II) and Ru(III) centres has been characterised for a variety of mononuclear organo-Ru complexes.[50-52] For example, the crystal structures of Ru(II) complexes coordinated to η^6-arene moieties and *L*-methionine (via bidentate or tridentate binding) reported by Ji *et al.* indicate interatomic distances for Ru—N, Ru—O, and Ru—S between 2.10–2.12 Å, 2.08–2.09 Å, and 2.38–2.39 Å, respectively.[52] Additional computational models could be constructed to simulate the multiple scattering interactions for reduced mononuclear Ru complexes coordinated to H_2O/OH^-, NH_3, and *L*-methionine or *L*-cysteine, however, the inability to readily distinguish between N and O, or between S and Cl backscatterers remains a significant limitation. Hence, synthesis of model mononuclear Ru metabolites and further characterisation by

complementary techniques, such as XRD and proton NMR spectroscopy, would be necessary to further explore these hypotheses.

Using Fit B, EXAFS curve-fitting of blood plasma from the Ru360 treatment was attempted, however, the poor signal-to-noise in this data created further interference and peak broadening in the Fourier transform (**Table S1**, **Figure S15**). Negligible signal was obtained for the corresponding RBC sample (**Figure S16**), indicating that the degraded Ru360 products (mononuclear Ru) were not effectively taken up by RBCs. Previous permeability studies in cancer cell models have demonstrated that unlike Ru265, the uptake of Ru360' is unaffected by overexpression of OCT3, leading to the postulation that Ru360' and/or its reduction products are not efficient substrates for this key transporter.[22] Amongst the polyspecific cation transporters (OCT1-3), OCT3 exhibits the broadest expression in mammalian tissues, occurring most abundantly in the skeletal muscle, liver, heart, and placenta in humans.[33] However, the expression of OCT1-3 has not been reported in human RBCs, therefore, we anticipate that uptake of Ru265' may occur via an alternative cellular transport mechanism. Collectively, these findings highlight that the oxo-bridged MCU inhibitor lacks adequate redox stability which subsequently impacts its permeability to both erythrocytes and the cell membranes of target tissues.

Table 3. EXAFS curve-fitting parameters for Ru265 and Ru360 in whole blood.[a] Samples were incubated at 37 °C for 1 h (final concentration, 0.1 mM Ru265 or Ru360 and 1% DMSO).

Fit[b]	Sample	Path[c]	N	R (Å)	σ^2 (Å^2)	ΔE_0 (eV)	F[d]
A	Ru265	Ru—N_{br}	1	1.738(1)	0.0007(1)[e]	-5.0(3)	0.3810
		Ru···Ru	1,2,1	3.477(1)	0.0015(1)		
		Ru—N	4	2.108(3)	0.0015[f]		
		Ru—O	1	2.091(9)	0.0020(9)		
		+8 additional unlisted single and multiple scattering shells[g]					
A	Ru360	Ru—O_{br}	1	1.802(8)	0.004(1)	-6.9(6)	0.6231
		Ru···Ru	1,2,1	3.694(6)[h]	0.0072(6)[h]		
		Ru—N	4	2.122(3)	0.0027(3)		
		Ru—O	1	2.01(1)	0.004(1)		
		+11 additional unlisted single and multiple scattering shells[g]					
B	Ru360	Ru—O_{br}	1	1.807(9)	0.005(1)	-6.5(5)	0.6193
		Ru···Ru	1,2,1	3.695(6)[h]	0.0072(5)[h]		
		Ru—N	4	2.100(3)	0.0030(3)		
		Ru—S/Cl	1	2.319(9)	0.007(1)		
		+14 additional unlisted single and multiple scattering shells[g]					
C	Ru360	Ru—O_{br}	1	1.796(8)	0.0040(9)	-10.0(5)	0.6115
		Ru···Ru	1,2,1	3.684(6)[h]	0.0073(6)[h]		
		Ru—N/O	3	2.103(4)	0.0032(4)		
		Ru—N/O	1	2.03(1)	0.005(2)		
		Ru—S/Cl	1	2.277(9)	0.006(1)		
		+12 additional unlisted single and multiple scattering shells[g]					

[a] Coordination numbers (N), interatomic distances (R), Debye-Waller factors (σ^2, mean-square deviations in interatomic distance), and threshold energy shifts (ΔE_0). The values in parentheses are the estimated standard deviations in the last digit obtained from the diagonal elements of the covariance matrix. Note that the accuracies are somewhat larger than the precisions, typically ± 0.02 Å for R and ± 20% for N and σ^2.

[b] Alternative fits A (H_2O or OH^- axial ligands), B (OH^- replaced with axial S/Cl ligand), and C (combination of 3 x NH_3, 1 x O-coordinating ligand, and 1 x S-coordinating ligand). These fits have approximately equivalent fit errors for Ru360 in whole blood.

[c] All paths terminate at the originating Ru atom (not indicated). Note that EXAFS cannot readily distinguish between scatterers of similar atomic number (e.g. S/Cl or N/O). Assignments of Ru—N (from NH_3) ligands and Ru—O (from H_2O or OH^- axial ligands) are based on the consistency of N and R with the crystallographic models.

[d] The fit-error function (F) is defined by $F = \left(\sum k^6 \left(\chi(k)_{cald} - \chi(k)_{expt}\right)^2 / \sum \chi(k)^2_{expt}\right)^{1/2}$, where $\chi(k)$ are the EXAFS oscillations and *k* is the photoelectron wavenumber given by $k = \left(\left(2m_e/\hbar^2\right)\left(E - E_0\right)\right)^{1/2}$.

[e] Debye-Waller factor below the typical chemically reasonable lower limit of 0.0015 Å^2 is accepted for these features given the rigidity of the Ru—N—Ru backbone.

[f] For Ru—N (NH_3), the Debye-Waller factor was constrained to the chemically reasonable lower limit (0.0015 Å^2). Unconstrained the value converged at 0.0012 Å^2.

[g] Paths include the single scattering path Ru···N (NH_3 ligands on adjacent Ru atom) and multiple scattering paths to the distant axial ligand across the Ru—N—Ru or Ru—O—Ru backbone.

[h] In this sample where the dinuclear Ru360 complex showed degradation, Ru—O_{br} was unlinked from Ru···Ru paths (1:2 proportionality in Debye-Waller factor no longer maintained).

3.3 Comments on data quality

With respect to the data described above, we note that all EXAFS spectra were collected across a larger *k*-range (k_{max} = 13.0 – 15.8 Å^{-1}), however, the data was consistently truncated to k_{max} = 12.5 Å^{-1} to eliminate poor signal-to-noise which exacerbated with increasing *k*-range. This was particularly evident for the biological samples where the concentrations of Ru265 and Ru360 were less than 1 mM. Although extension of the *k*-range provides more data points for structural determination and affords greater bond resolution and accuracy in the assignment of interatomic distances, interpretations of the data to k_{max} = 12.5 Å^{-1} provided sufficient detail to identify the Ru—X—Ru backbone and characterise whether these dinuclear Ru compounds remained intact. This is emphasised in the comparison of the curve-fitting parameters for EXAFS truncated to k_{max} = 12.5 Å^{-1} or extended to k_{max} = 15.0 Å^{-1} for Ru265 standards with the best quality data (**Table S2** and **Figures S17-S18**). In these samples, the bond distances determined for all key paths are consistent for both *k*-ranges, with the two fits for each sample giving similar weighted fit-errors (ΔF-factor ± 3%).

4 Conclusions

Supporting previous investigations of the redox stability of these dinuclear Ru compounds, our EXAFS results demonstrate that Ru265 maintains stability in buffer and saline solutions at physiological pH and is resistant to reduction by GSH (5 molar equivalents). Furthermore, EXAFS curve-fitting data indicates that Ru265 remains intact in human whole blood after 1 h incubation at 37 °C and exhibits appreciable uptake into RBCs. In contrast, Ru360 was shown to be degraded in physiological saline containing 10% DMSO at room temperature, with further deterioration occurring after incubation in blood. Thus, our data highlights the utility of EXAFS analysis for the elucidation of valuable structural information regarding these dinuclear Ru compounds in biological samples. Specifically, multiple scattering EXAFS curve-fitting enabled sensitive monitoring of the absorber-backscatterer interactions across the Ru—X—Ru backbone. This sensitivity, accompanied by the simple sample preparation protocols and rapid freezing in LN2, allowed us to accurately capture and examine changes in ligand coordination and complex degradation within a narrow window of exposure and treatment. Despite these advantages, given the inability to distinguish between backscatterers with

similar atomic number (N/O and S/Cl), the structures and coordination environment(s) of Ru360 degradation products (mononuclear Ru species) could not be determined. Additional models and supporting crystallographic and spectroscopic data, coupled with chromatographic separation techniques, are required to adequately resolve and characterise these mononuclear species. Nevertheless, further EXAFS studies, examining a broader range of biologically relevant conditions, are also necessary to fully evaluate the *in vitro* and *in vivo* redox activities and stability of Ru265. These insights may then be used inform the continued development and optimisation of dinuclear metal-based therapeutics.

Supporting Information: ^{1}H NMR and UV-Vis characterisation of Ru265 in saline/DMSO; additional EXAFS curve fitting plots and tables; XAS edge spectrum for Ru360 in RBCs (pdf).

Acknowledgements

This research was conducted at the X-ray Absorption Spectroscopy (XAS) beamline at the Australian Synchrotron (AS), Victoria, Australia, with merit beamtime funded by the Australian Nuclear Science and Technology Organisation (ANSTO). Research conducted in the lab of Justin Wilson was supported by funding from the United States National Science Foundation (Award No. CHE-2414429).

References

(1) Vandecasteele, G.; Szabadkai, G.; Rizzuto, R. Mitochondrial Calcium Homeostasis: Mechanisms and Molecules. *IUBMB Life* **2001**, *52* (3-5), 213-219. DOI: 10.1080/15216540152846028
(2) Williams, G. S. B.; Boyman, L.; Chikando, A. C.; Khairallah, R. J.; Lederer, W. J. Mitochondrial calcium uptake. *Proc Nat Acad Sci* **2013**, *110* (26), 10479-10486. DOI: 10.1073/pnas.1300410110
(3) Dhaouadi, N.; Vitto, V. A. M.; Pinton, P.; Galluzzi, L.; Marchi, S. Ca^{2+} signaling and cell death. *Cell Calcium* **2023**, *113*, 102759. DOI: 10.1016/j.ceca.2023.102759
(4) Kamer, K. J.; Mootha, V. K. The molecular era of the mitochondrial calcium uniporter. *Nat Rev Mol Cell Biol* **2015**, *16* (9), 545-553. DOI: 10.1038/nrm4039
(5) Márta, K.; Hasan, P.; Rodríguez-Prados, M.; Paillard, M.; Hajnóczky, G. Pharmacological inhibition of the mitochondrial Ca^{2+} uniporter: Relevance for pathophysiology and human therapy. *J Mol Cell Cardiol* **2021**, *151*, 135-144. DOI: 10.1016/j.yjmcc.2020.09.014
(6) Novorolsky, R. J.; Nichols, M.; Kim, J. S.; Pavlov, E. V.; J, J. W.; Wilson, J. J.; Robertson, G. S. The cell-permeable mitochondrial calcium uniporter inhibitor Ru265 preserves cortical neuron respiration after lethal oxygen glucose deprivation and reduces hypoxic/ischemic brain injury. *J Cereb Blood Flow Metab* **2020**, *40* (6), 1172-1181. DOI: 10.1177/0271678x20908523
(7) Krieger, C.; Duchen, M. R. Mitochondria, Ca^{2+} and neurodegenerative disease. *Eur J Pharmacol* **2002**, *447* (2-3), 177-188.
(8) Pchitskaya, E.; Popugaeva, E.; Bezprozvanny, I. Calcium signaling and molecular mechanisms underlying neurodegenerative diseases. *Cell Calcium* **2018**, *70*, 87-94. DOI: 10.1016/j.ceca.2017.06.008
(9) Rossi, A.; Pizzo, P.; Filadi, R. Calcium, mitochondria and cell metabolism: A functional triangle in bioenergetics. *Biochim Biophys Acta Mol Cell Res* **2019**, *1866* (7), 1068-1078.
(10) Liu, Y.; Jin, W.; Zhou, H.; Wang, X.; Ren, H.; Yang, X.; Luo, K.; Dou, X. Role of mitochondrial Ca^{2+} in stroke: From molecular mechanism to treatment strategy (Review). *Mol Med Rep* **2025**, *32* (4). DOI: 10.3892/mmr.2025.13636
(11) Kwong, J. Q. The mitochondrial calcium uniporter in the heart: energetics and beyond. *J Physiol* **2017**, *595* (12), 3743-3751. DOI: 10.1113/jp273059
(12) Murphy, E.; Liu, J. C. Mitochondrial calcium and reactive oxygen species in cardiovascular disease. *Cardiovasc Res* **2022**, *119* (5), 1105-1116. DOI: 10.1093/cvr/cvac134
(13) Paupe, V.; Prudent, J. New insights into the role of mitochondrial calcium homeostasis in cell migration. *Biochem Biophys Res Commun* **2018**, *500* (1), 75-86. DOI: 10.1016/j.bbrc.2017.05.039

(14) Vultur, A.; Gibhardt, C. S.; Stanisz, H.; Bogeski, I. The role of the mitochondrial calcium uniporter (MCU) complex in cancer. *Pflugers Arch Euro J Physiol* **2018**, *470* (8), 1149-1163. DOI: 10.1007/s00424-018-2162-8
(15) Woods, J. J.; Wilson, J. J. Inhibitors of the mitochondrial calcium uniporter for the treatment of disease. *Curr Opin Chem Biol* **2020**, *55*, 9-18. DOI: 10.1016/j.cbpa.2019.11.006
(16) Giorgi, C.; Agnoletto, C.; Bononi, A.; Bonora, M.; De Marchi, E.; Marchi, S.; Missiroli, S.; Patergnani, S.; Poletti, F.; Rimessi, A.; Suski, J. M.; Wieckowski, M. R.; Pinton, P. Mitochondrial calcium homeostasis as potential target for mitochondrial medicine. *Mitochondrion* **2012**, *12* (1), 77-85. DOI: 10.1016/j.mito.2011.07.004
(17) Nemani, N.; Shanmughapriya, S.; Madesh, M. Molecular regulation of MCU: Implications in physiology and disease. *Cell Calcium* **2018**, *74*, 86-93. DOI: 10.1016/j.ceca.2018.06.006
(18) Arduino, D. M.; Perocchi, F. Pharmacological modulation of mitochondrial calcium homeostasis. *J Physiol* **2018**, *596* (14), 2717-2733. DOI: 10.1113/jp274959
(19) Kon, N.; Murakoshi, M.; Isobe, A.; Kagechika, K.; Miyoshi, N.; Nagayama, T. DS16570511 is a small-molecule inhibitor of the mitochondrial calcium uniporter. *Cell Death Discov* **2017**, *3*, 17045. DOI: 10.1038/cddiscovery.2017.45
(20) Arduino, D. M.; Wettmarshausen, J.; Vais, H.; Navas-Navarro, P.; Cheng, Y.; Leimpek, A.; Ma, Z.; Delrio-Lorenzo, A.; Giordano, A.; Garcia-Perez, C.; Médard, G.; Kuster, B.; García-Sancho, J.; Mokranjac, D.; Foskett, J. K.; Alonso, M. T.; Perocchi, F. Systematic Identification of MCU Modulators by Orthogonal Interspecies Chemical Screening. *Mol Cell* **2017**, *67* (4), 711-723.e717. DOI: 10.1016/j.molcel.2017.07.019
(21) Woods, J. J.; Nemani, N.; Shanmughapriya, S.; Kumar, A.; Zhang, M.; Nathan, S. R.; Thomas, M.; Carvalho, E.; Ramachandran, K.; Srikantan, S.; Stathopulos, P. B.; Wilson, J. J.; Madesh, M. A Selective and Cell-Permeable Mitochondrial Calcium Uniporter (MCU) Inhibitor Preserves Mitochondrial Bioenergetics after Hypoxia/Reoxygenation Injury. *ACS Cent Sci* **2019**, *5* (1), 153-166. DOI: 10.1021/acscentsci.8b00773
(22) Woods, J. J.; Lovett, J.; Lai, B.; Harris, H. H.; Wilson, J. J. Redox stability controls the cellular uptake and activity of ruthenium-based inhibitors of the mitochondrial calcium uniporter (MCU). *Angew Chem Int Ed* **2020**, *59* (16), 6482-6491. DOI: 10.1002/anie.202000247
(23) Santo-Domingo, J.; Vay, L.; Hernández-Sanmiguel, E.; Lobatón, C. D.; Moreno, A.; Montero, M.; Alvarez, J. The plasma membrane Na^+/Ca^{2+} exchange inhibitor KB-R7943 is also a potent inhibitor of the mitochondrial Ca^{2+} uniporter. *Br J Pharmacol* **2007**, *151* (5), 647-654. DOI: 10.1038/sj.bjp.0707260
(24) Antonenko, Y. N.; Rokitskaya, T. I.; Cooper, A. J.; Krasnikov, B. F. Minocycline chelates Ca^{2+}, binds to membranes, and depolarizes mitochondria by formation of Ca^{2+}-dependent ion channels. *J Bioenerg Biomembr* **2010**, *42* (2), 151-163. DOI: 10.1007/s10863-010-9271-1
(25) Thu, V. T.; Kim, H. K.; Long le, T.; Lee, S. R.; Hanh, T. M.; Ko, T. H.; Heo, H. J.; Kim, N.; Kim, S. H.; Ko, K. S.; Rhee, B. D.; Han, J. NecroX-5 prevents hypoxia/reoxygenation injury by inhibiting the mitochondrial calcium uniporter. *Cardiovasc Res* **2012**, *94* (2), 342-350. DOI: 10.1093/cvr/cvs122
(26) Emerson, J.; Clarke, M.; Ying, W. L.; Sanadi, D. R. The component of" ruthenium red" responsible for inhibition of mitochondrial calcium ion transport. Spectra, electrochemistry, and aquation kinetics. Crystal structure of. mu.-O-$[(HCO_2)(NH_3)_4Ru]_2Cl_3$. *J Am Chem Soc* **1993**, *115* (25), 11799-11805.
(27) Matlib, M. A.; Zhou, Z.; Knight, S.; Ahmed, S.; Choi, K. M.; Krause-Bauer, J.; Phillips, R.; Altschuld, R.; Katsube, Y.; Sperelakis, N. Oxygen-bridged dinuclear ruthenium amine complex specifically inhibits Ca^{2+} uptake into mitochondria in vitroand in situ in single cardiac myocytes. *J of Biol Chem* **1998**, *273* (17), 10223-10231. DOI: 10.1074/jbc.273.17.10223
(28) Abramov, A. Y.; Duchen, M. R. Mechanisms underlying the loss of mitochondrial membrane potential in glutamate excitotoxicity. *Biochim Biophys Acta* **2008**, *1777* (7-8), 953-964. DOI: 10.1016/j.bbabio.2008.04.017
(29) de J García-Rivas, G.; Carvajal, K.; Correa, F.; Zazueta, C. Ru360, a specific mitochondrial calcium uptake inhibitor, improves cardiac post-ischaemic functional recovery in rats *in vivo*. *Br J Pharmacol* **2006**, *149* (7), 829-837. DOI: 10.1038/sj.bjp.0706932

(30) Woods, J. J.; Rodriguez, M. X.; Tsai, C.-W.; Tsai, M.-F.; Wilson, J. J. Cobalt amine complexes and Ru265 interact with the DIME region of the mitochondrial calcium uniporter. *Chem Commun* **2021**, *57* (50), 6161-6164. DOI: 10.1039/D1CC01623G
(31) Wu, X.; Kekuda, R.; Huang, W.; Fei, Y.-J.; Leibach, F. H.; Chen, J.; Conway, S. J.; Ganapathy, V. Identity of the organic cation transporter OCT3 as the extraneuronal monoamine transporter (uptake2) and evidence for the expression of the transporter in the brain. *J Biol Chem* **1998**, *273* (49), 32776-32786. DOI: 10.1074/jbc.273.49.32776
(32) Vialou, V.; Amphoux, A.; Zwart, R.; Giros, B.; Gautron, S. Organic cation transporter 3 (Slc22a3) is implicated in salt-intake regulation. *J Neurosci* **2004**, *24* (11), 2846-2851. DOI: 10.1523/JNEUROSCI.5147-03.2004
(33) Koepsell, H.; Lips, K.; Volk, C. Polyspecific Organic Cation Transporters: Structure, Function, Physiological Roles, and Biopharmaceutical Implications. *Pharm Res* **2007**, *24* (7), 1227-1251. DOI: 10.1007/s11095-007-9254-z
(34) Harris, H. H.; George, G. N.; Rajagopalan, K. V. High-Resolution EXAFS of the Active Site of Human Sulfite Oxidase: Comparison with Density Functional Theory and X-ray Crystallographic Results. *Inorg Chem* **2006**, *45* (2), 493-495. DOI: 10.1021/ic0512274
(35) Cotelesage, J. J.; Pushie, M. J.; Grochulski, P.; Pickering, I. J.; George, G. N. Metalloprotein active site structure determination: synergy between X-ray absorption spectroscopy and X-ray crystallography. *J Inorg Biochem* **2012**, *115*, 127-137. DOI: 10.1016/j.jinorgbio.2012.06.019
(36) Nathan, S. R.; Pino, N. W.; Arduino, D. M.; Perocchi, F.; MacMillan, S. N.; Wilson, J. J. Synthetic Methods for the Preparation of a Functional Analogue of Ru360, a Potent Inhibitor of Mitochondrial Calcium Uptake. *Inorg Chem* **2017**, *56* (6), 3123-3126. DOI: 10.1021/acs.inorgchem.6b03108
(37) George, G. N.; Pickering, I. J. EXAFSPAK: A suite of computer programs for analysis of X-ray absorption spectra. Stanford Synchrotron Radiation Laboratory, Stanford, CA, USA: 1995.
(38) Rehr, J. J.; Albers, R. C. Theoretical approaches to x-ray absorption fine structure. *Reviews of Modern Physics* **2000**, *72* (3), 621-654. DOI: 10.1103/RevModPhys.72.621
(39) Adeniyi, A. A.; Ajibade, P. A. Exploring the Ruthenium-Ligands Bond and Their Relative Properties at Different Computational Methods. *J Chem* **2016**, *2016* (1), 3672062. DOI: 10.1155/2016/3672062
(40) Gironi, B.; Kahveci, Z.; McGill, B.; Lechner, B.-D.; Pagliara, S.; Metz, J.; Morresi, A.; Palombo, F.; Sassi, P.; Petrov, P. G. Effect of DMSO on the Mechanical and Structural Properties of Model and Biological Membranes. *Biophys J* **2020**, *119* (2), 274-286. DOI: 10.1016/j.bpj.2020.05.037
(41) Rammler, D. H.; Zaffaroni, A. Biological implications of DMSO based on a review of its chemical properties. *Ann NY Acad Sci* **1967**, *141* (1), 13-23. DOI: 10.1111/j.1749-6632.1967.tb34861.x
(42) Williams, A. C.; Barry, B. W. Penetration enhancers. *Adv Drug Deliv Rev* **2012**, *64*, 128-137. DOI: 10.1016/j.addr.2012.09.032
(43) Henn, M.; Alessio, E.; Mestroni, G.; Calligaris, M.; Attia, W. M. Ruthenium(II)-dimethyl sulfoxide complexes with nitrogen ligands: synthesis, characterization and solution chemistry. The crystal structures of *cis*,*fac*-$RuCl_2(DMSO)_3(NH_3)$ and *trans*,*cis*,*cis*-$RuCl_2(DMSO)_2(NH_3)_2{\cdot}H_2O$. *Inorg Chim Acta* **1991**, *187* (1), 39-50. DOI: 10.1016/S0020-1693(00)82975-8
(44) Turel, I.; Pečanac, M.; Golobič, A.; Alessio, E.; Serli, B.; Bergamo, A.; Sava, G. Solution, solid state and biological characterization of ruthenium(III)-DMSO complexes with purine base derivatives. *J Inorg Biochem* **2004**, *98* (2), 393-401. DOI: 10.1016/j.jinorgbio.2003.12.001
(45) Marr, Z. Y.; Thapa Magar, R.; Fournier, B.; Benedict, J. B.; Rack, J. J. Photocrystallography of $[Ru(bpy)_2(dmso)_2]^{2+}$ reveals an O-bonded metastable state. *Chem Sci* **2023**, *14* (26), 7279-7284, 10.1039/D3SC01526B. DOI: 10.1039/D3SC01526B
(46) Calligaris, M. Structure and bonding in metal sulfoxide complexes: an update. *Coord Chem Rev* **2004**, *248* (3), 351-375. DOI: 10.1016/j.ccr.2004.02.005
(47) Yi, X.; Liu, M.; Luo, Q.; Zhuo, H.; Cao, H.; Wang, J.; Han, Y. Toxic effects of dimethyl sulfoxide on red blood cells, platelets, and vascular endothelial cells in vitro. *FEBS Open Bio* **2017**, *7* (4), 485-494. DOI: 10.1002/2211-5463.12193

(48) Verheijen, M.; Lienhard, M.; Schrooders, Y.; Clayton, O.; Nudischer, R.; Boerno, S.; Timmermann, B.; Selevsek, N.; Schlapbach, R.; Gmuender, H.; Gotta, S.; Geraedts, J.; Herwig, R.; Kleinjans, J.; Caiment, F. DMSO induces drastic changes in human cellular processes and epigenetic landscape in vitro. *Sci Rep* **2019**, *9* (1), 4641. DOI: 10.1038/s41598-019-40660-0
(49) Xu, P.; Swain, S.; Novorolsky, R. J.; Garcia, E.; Huang, Z.; Snutch, T. P.; Wilson, J. J.; Robertson, G. S.; Renden, R. B. The mitochondrial calcium uniporter inhibitor Ru265 increases neuronal excitability and reduces neurotransmission via off-target effects. *Br J Pharmacol* **2024**, *181* (18), 3503-3526. DOI: 10.1111/bph.16425
(50) Sheldrick, W. S.; Exner, R. Synthesis and structural characterization of ruthenium(II) complexes of histidine and methionine derivatives. *Inorg Chim Acta* **1992**, *195* (1), 1-9. DOI: 10.1016/S0020-1693(00)83844-X
(51) Filho, J. R. O.; Silva, W. C.; Pereira, J. C. M.; Franco, D. W. Binding of cysteine and glutathione to Ru(II) and Ru(III) centers: Formation and products reactivities. *Inorg Chim Acta* **2006**, *359* (9), 2888-2895. DOI: 10.1016/j.ica.2005.11.044
(52) Ji, J.; Chen, C.; Jia, A.-Q.; Shi, H.-T.; Zhang, Q.-F. Syntheses, structures and photocatalytic properties of ruthenium complexes bearing L-methionine ligands. *J Organomet Chem* **2020**, *907*, 121078. DOI: 10.1016/j.jorganchem.2019.121078